

Propulsive Forces on the Flagellum during Locomotion of *Chlamydomonas reinhardtii*

P. V. Bayly,^{†*} B. L. Lewis,[‡] E. C. Ranz,[†] R. J. Okamoto,[†] R. B. Pless,[§] and S. K. Dutcher[†]

[†]Department of Mechanical Engineering and Materials Science, Washington University in St. Louis, St. Louis, Missouri; [‡]Department of Genetics, Washington University School of Medicine, St. Louis, Missouri; and [§]Department of Computer Science and Engineering, Washington University in St. Louis, St. Louis, Missouri

ABSTRACT The distributed propulsive forces exerted on the flagellum of the swimming alga *Chlamydomonas reinhardtii* by surrounding fluid were estimated from experimental image data. Images of unflagellate mutant *Chlamydomonas* cells were obtained at 350 frames/s with 125-nm spatial resolution, and the motion of the cell body and the flagellum were analyzed in the context of low-Reynolds-number fluid mechanics. Wild-type unflagellate cells, as well as unflagellate cells lacking inner dynein arms (*ida3*) or outer dynein arms (*oda2*) were studied. *Ida3* cells exhibit stunted flagellar waveforms, whereas *oda2* cells beat with lower frequency. Image registration and sorting algorithms provided high-resolution estimates of the motion of the cell body, as well as detailed kinematics of the flagellum. The swimming cell was modeled as an ellipsoid in Stokes flow, propelled by viscous forces on the flagellum. The normal and tangential components of force on the flagellum (f_N and f_T) were related by resistive coefficients (C_N and C_T) to the corresponding components of velocity (V_N and V_T). The values of these coefficients were estimated by satisfying equilibrium requirements for force and torque on the cell. The estimated values of the resistive coefficients are consistent among all three genotypes and similar to theoretical predictions.

INTRODUCTION

Cilia and flagella are thin cellular organelles that bend actively to move fluid or to propel the cell. The highly regulated movements of cilia are essential for the normal function of many organs. Disorders of ciliary motion (ciliopathies) cause congenital defects, chronic respiratory tract infections, and infertility. The axoneme (the cytoskeletal structure of cilia and flagella) is known to consist of a 9 + 2 arrangement of microtubule doublets actuated by motor proteins: inner and outer dynein arms. Dynein arms are minus-end-directed microtubule motors that generate flagellar and ciliary motion by conversion of ATP hydrolysis into microtubule sliding (1). Despite its importance, and years of intense study, the precise mechanism and coordination of the ciliary or flagellar beat remain incompletely understood.

Previous studies suggest that the timing and magnitude of dynein activity is modulated by mechanical feedback. Internal stresses or strains in the axoneme may limit attachment of dynein arms (2,3) or affect their stepping rate (4). The forces exerted by the surrounding fluid on the moving flagellum are important components of axonemal kinetics; these forces must be estimated accurately to clarify the details of dynein activity in the flagellar beat.

The unicellular alga *Chlamydomonas reinhardtii* provides an excellent experimental system for the study of ciliary and flagellar kinetics. The *Chlamydomonas* flagellum and the human cilium share a common 9 + 2 axonemal structure, in which dynein motors act in coordination to produce asymmetric, propulsive waveforms. (The analogy is not exact;

for example, the beat frequency of the cilium is much lower, ~10 Hz, compared to 60–70 Hz in the *Chlamydomonas* flagellum). *Chlamydomonas* can be manipulated genetically to produce mutations analogous to those seen in human disease. Although *Chlamydomonas* is normally biflagellate, most of the early analysis of the waveform of *Chlamydomonas* flagella was aided by the *uni1* mutant strain (5). The *uni1* mutant strain assembles only one flagellum, and *uni1* cells that use the breast-stroke or forward-movement mode rotate approximately in place (6). In pioneering work, Brokaw and Luck (7) photographed *uni1* flagella using dark-field optics with flash illumination at 300 Hz. This method provided four to eight images per beat, which were analyzed in detail to characterize the flagellar waveform.

Qualitative differences in waveform among different *Chlamydomonas* mutants have been documented in a number of studies (8–10) since the seminal work of Brokaw, Kamiya, and collaborators (6,7,11,12). Mutations in at least 10 genes in *Chlamydomonas* result in the loss of the outer dynein arms, which are located on the outer circumference of the doublet microtubules. Loss of the outer dynein arms affects the frequency of the beat (12,13). The inner dynein arms, which are located on the inner circumference of the doublets, are heterogeneous (14). The loss of a particular inner arm, I1, or *f*-dynein, is known to affect the waveform (12) but not the beat frequency. The I1 inner dynein is a two-headed dynein that is found along the length of the axoneme and appears as a trilobed structure by electron microscopy (15).

The force exerted by dynein arms deforms elastic components of the flagellum and moves the surrounding fluid. The opposing force of the fluid on the flagellum propels the cell

Submitted February 3, 2011, and accepted for publication May 4, 2011.

*Correspondence: baylyp@seas.wustl.edu

Editor: Charles W. Wolgemuth.

© 2011 by the Biophysical Society
0006-3495/11/06/2716/10 \$2.00

doi: 10.1016/j.bpj.2011.05.001

forward. Models of flagellar activity that focus on flagellar dynamics typically treat the fluid forces simplistically. The Reynolds number of the flow is very low, so that inertial effects are safely neglected. In resistive-force theory (16), the normal and tangential components of force on the flagellum are simply scalar multiples of the normal and tangential components of its velocity. Lighthill (17) criticized this approach, but also suggested improved formulas for the coefficients that relate force to velocity. One obvious effect that is neglected in resistive-force theory is the interaction between the flagellar motion and the cell body (the cell body swims upstream against the flow induced by the flagellum). Johnson and Brokaw (18) explored the ability of resistive-force theory and slender-body theory (19,20) to predict behavior observed in simulations of cell motion.

Despite intense study of *Chlamydomonas reinhardtii*, the viscous forces on its flagellum remain uncertain. Direct measurement of flagellar force would be extremely difficult, but in principle, viscous forces may be estimated from kinematic measurements, together with equations of low-Reynolds-number fluid mechanics. However, reliable estimation of instantaneous velocities and forces by this approach requires a description of the flagellar waveform with excellent spatial and temporal resolution. In this study, we estimate propulsive fluid forces from the motion of cell body and flagellum in cells of uniflagellate mutant background (wild-type), as well as in uniflagellate double-mutant cells that lack outer dynein arms (*oda2*) or the II-dynein complex (*ida3*). Digital image analysis and sorting algorithms are developed to describe cell-body and flagellar kinematics and kinetics quantitatively, with high spatial and temporal resolution. The flagellar motion of each genotype is distinct, providing a robust evaluation of the simple resistive-force theory.

MATERIALS AND METHODS

Cell cultures and genetics

Chlamydomonas reinhardtii cells were grown as in previous studies (21). The uniflagellate mutant strains, *uni1-2*, *uni1-2*; *ida3*, and *uni1-2*; *oda2* were generated from meiotic crosses (22). The *uni1-2* strain was chosen for its ability to rotate approximately in place, which allows images to be acquired for relatively long periods (23). The *uni1-2* exhibits a beat frequency of 60–70 Hz, similar to biflagellate wild-type cells, and typically rotates at 4–5 revolutions/s. Mutants displaying the *ida3* or *oda2* phenotypes were selected from meiotic progeny of a *uni1-2* by *ida3* cross or *uni1-2* by *oda2* cross by screening for cells that rotated more slowly than the *uni1-2* cells. Selected double-mutant strains were confirmed by backcrossing with wild-type cells and analyzing the meiotic progeny. Cells were allowed to grow for 48 h in Sager and Granick rich liquid medium (24) at 25°C, in constant light from fluorescent bulbs (GE Daylight 20W F20T12D, General Electric, Fairfield, CT) with irradiance equal to 3100 ergs/cm²/s before images were acquired.

Video microscopy

All bright-field microscopy was carried out in a climate-controlled room maintained at 21°C. For each video, 20 μ L from a liquid culture were pipet-

ted onto an acid-washed slide and an 18 \times 18 mm coverslip was placed for viewing under a Zeiss Universal Microscope (Carl Zeiss, Oberkochen, Germany) with either 63 \times Planapo or 100 \times Neofluar oil-immersion objective lenses. The light source was a standard mercury arc lamp (HBO 100, Carl Zeiss). As soon as a single, rotating cell was brought into focus, microscope settings were adjusted to provide the greatest contrast between the flagellum and background. The separation between the slide and coverslip is estimated to be \sim 60 μ m (20 μ L vol/324 mm² area). The distance of rotating *uni1-2* *Chlamydomonas* from the bottom of the chamber was estimated using a microscope with a z-axis readout, by focusing first on stationary cells stuck to the bottom slide, then on nearby swimming cells. We found that the majority of swimming cells centered within 4–8 μ m from the surface of the bottom slide, consistent with the inability of *uni1-2* cells to overcome gravity.

Videos were made using the Dragonfly Express IEEE-1394b Digital Camera System and FlyCapture software (Point Gray Research, Scottsdale, AZ). Videos were captured at 350 frames/s (2.85 ms/frame) with 320 \times 240 pixels/image. From each video, a sequence of 200 consecutive frames (0.57 s) was stored as a stack of images: a three-dimensional array (320 \times 240 \times 200) of intensity values. The width of each square pixel in this array was 125 nm (0.125 μ m) in the image plane. Sample images are shown in Fig. 1 (upper row) (also see Movie S1 in the Supporting Material). Video data were analyzed with custom programs written in MATLAB (The Mathworks, Natick, MA).

Flagellar kinematics

The kinematic analysis of the flagellum has been described in detail previously (25). The four major steps are summarized here (also see Supporting Material). First, the rigid-body motion of the cell body (Fig. 1, upper row) is characterized by digital image registration (26) and subtracted so that the flagellar motion can be described with respect to a body-fixed reference frame, $G_{x'y'}$ (Figs. 1, middle and bottom rows, and 2, a and b, and Movie

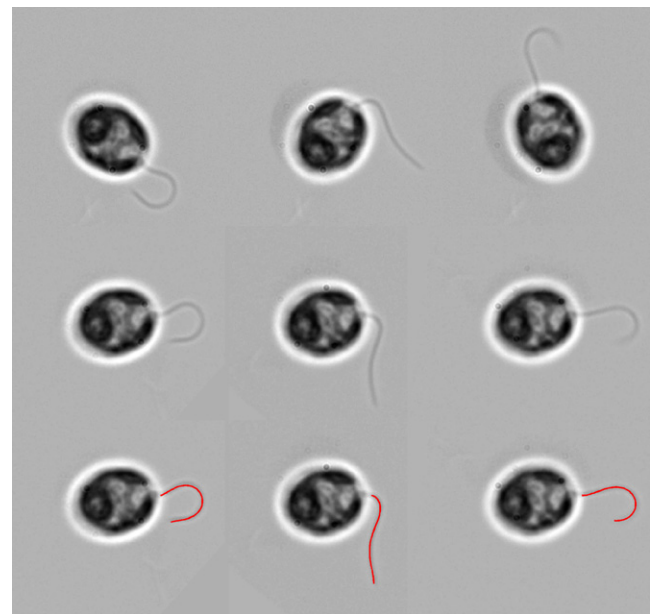


FIGURE 1 (Top row) Video images of wild-type uniflagellate *Chlamydomonas* cells swimming. (Middle row) Corresponding images after removing rigid-body motion of the cell body, so that the motion of the flagellum is seen with respect to a frame of reference fixed to the cell. (Bottom row) Superimposed curves with the mathematical representation of the flagellum by a smooth surface of its tangent angle, θ (s, τ). See also Movie S1, Movie S2, and Movie S3.

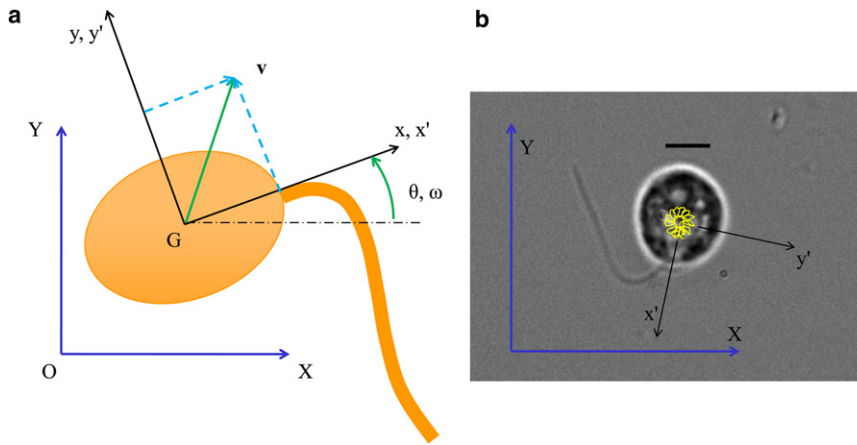


FIGURE 2 (a) Schematic diagram of the swimming *Chlamydomonas* showing the laboratory (O_{XY}) frame of reference and the cell-body-fixed ($G_{x'y'}$) frame of reference. The body-fixed frame translates with velocity, v , and rotates with angular velocity, ω . The body-aligned frame, G_{xy} , is coincident with $G_{x'y'}$, but stationary. Velocity can be expressed with respect to either of the frames, O_{XY} or G_{xy} . (b) Image of a swimming *Chlamydomonas* cell with the measured trajectory of the centroid shown superimposed. The laboratory and body-fixed reference frames are also shown. Scale bar, $5 \mu\text{m}$.

S2). Next, the Cartesian (x', y') coordinates of pixels on the flagellum are identified with respect to the body-fixed frame. This provides a dense set of points (a point cloud) along the length of the flagellum. Flagellar point clouds are then sorted in order of their phase in the beat cycle. The point clouds describe the flagellum at a large number of times, but the basic time resolution is coarse relative to the period of motion, since the frame rate (350/s) is only five to six times the beat frequency (60–70 Hz for wild-type). However, the mismatch between beat frequency and sampling frequency, augmented by random small variations in beat frequency, causes the images to be distributed evenly over the beat cycle. A high-resolution representation of the beat can be obtained by sorting the coarse time samples in order of their phase in the cycle (Movie S3). Finally, the sorted flagellar points are fitted to a smooth, time-periodic surface representation of the flagellar beat, $\theta(s, \tau)$, which represents the angle of the tangent to the flagellum as a function of distance along the flagellum (s) and temporal position in the beat (τ).

From this surface representation, Eqs. 1a and 1b below are used to compute the Cartesian coordinates, in the body-fixed frame, of points on the fitted curve,

$$x'(s, \tau) = x'_0 + \int_0^s \cos \theta(\xi, \tau) d\xi, \quad (1a)$$

$$y'(s, \tau) = y'_0 + \int_0^s \sin \theta(\xi, \tau) d\xi; \quad (1b)$$

parameters of motion, such as curvature and curve propagation velocity can be extracted from the $\theta(s, \tau)$ surfaces. This method provides a kinematic description of the flagellum that is smooth and highly resolved in time and space, which allows accurate estimation of temporal derivatives (velocities), as well as spatial derivatives.

Kinematics and kinetics of the cell body

The measured linear and angular displacements (θ , X , and Y) of the cell body (obtained by digital image registration, as described above) are differentiated to obtain linear and angular velocities of the cell in the laboratory frame ($v_X = \frac{dX}{dt}$, $v_Y = \frac{dY}{dt}$, $\omega = \frac{d\theta}{dt}$). These kinematic variables are used to describe the forces on the cell body with respect to a body-aligned frame, G_{xy} , which is instantaneously aligned with the body-fixed frame, $G_{x'y'}$, but which has no linear or angular velocity itself. The velocities of the cell body in the body-aligned reference frame (G_{xy}) may be obtained by straightforward transformation of coordinates. Referring to Fig. 2 a, the body-fixed frame, $G_{x'y'}$, is central and aligned with the principal axes of the ellipsoidal cell. The x' -direction is parallel to the major axis; the y' -

direction is parallel to the minor axis of the ellipsoid in the image plane. At any instant, the origin of the body-aligned frame G_{xy} is also at the center of the cell, and its axes are coincident with those of $G_{x'y'}$ (i.e., $\mathbf{e}_x = \mathbf{e}_{x'}$ and $\mathbf{e}_y = \mathbf{e}_{y'}$). The components of linear velocity of the cell body with respect to the body-aligned frame are (Fig. 2)

$$v_x = v_X \cos \theta + v_Y \sin \theta, \quad (2a)$$

$$v_y = -v_X \sin \theta + v_Y \cos \theta. \quad (2b)$$

The initial estimates of velocity are then sorted to maintain correspondence with the position of the flagellum at the same instant (25) (also see Supporting Material). The sorted data are smoothed by application of a low-pass filter (noncausal, zero phase offset, with cut-off frequency equal to five times the beat frequency). Just as for the flagellum, the results are smooth estimates of the linear and angular velocities of the cell body, throughout a representative beat, with excellent temporal resolution.

The corresponding viscous forces on the cell body can be estimated from the formulas governing the motion of a sphere or an ellipsoid in Stokes flow. The equations of Stokes flow are linear, so that for a given combination of linear and angular velocities, the resultant force and moment can be obtained by superposition. Equations for ellipsoids have been obtained for many scenarios, beginning with the work of Oberbeck (27). Chwang and Wu (28) present the viscous drag and torque on a prolate ellipsoid as functions of the viscosity, μ , the major axis, a , the minor axis, b , and the eccentricity, $e = \sqrt{1 - b^2/a^2}$.

$$F_x = 6\pi\mu a v_x \times C_{F1}, \quad (3a)$$

$$F_y = 6\pi\mu a v_y \times C_{F2}, \quad (3b)$$

$$M_G = 8\pi\mu a b^2 \omega \times C_{F3}, \quad (3c)$$

where

$$C_{F1} = \frac{8}{3} e^3 \left[-2e + (1 + e^2) \ln \frac{1+e}{1-e} \right]^{-1}, \quad (3d)$$

$$C_{F2} = \frac{16}{3} e^3 \left[2e + (3e^2 - 1) \ln \frac{1+e}{1-e} \right]^{-1}, \quad (3e)$$

$$C_{F3} = \frac{4}{3} e^3 \left(\frac{2 - e^2}{1 - e^2} \right) \left[-2e + (1 + e^2) \ln \frac{1+e}{1-e} \right]^{-1}. \quad (3f)$$

Equations 3a and 3b (together with Eqs. 3d and 3e) govern the components of linear drag on the ellipsoid at very low Reynolds numbers. Equation 3c (with Eq. 3f) describes the relationship between torque and rotation of the prolate ellipsoid about its minor axis.

Forces on the flagellum

The force of the fluid on the flagellum is estimated from the simplest mathematical model, resistive-force theory (16). In resistive-force theory, the force/unit length is expressed in terms of normal and tangential components, f_N and f_T , which are obtained by multiplying the normal and tangential velocity components by coefficients C_N and C_T .

To estimate forces on the flagellum, the velocity of the flagellum with respect to the laboratory frame, and thus with respect to approximately quiescent fluid, is sought. First, the velocity of any point on the flagellum, with respect to the body-fixed frame, is obtained from the smoothed surface $\theta(s, \tau)$ using Eqs. 1a and 1b and

$$(\mathbf{v})_{Gx'y'} = \frac{dx'(s, t)}{dt} \mathbf{e}_x + \frac{dy'(s, t)}{dt} \mathbf{e}_y. \quad (4)$$

Then, the absolute velocity (with respect to the laboratory frame) is obtained by adding the linear velocity of the body-fixed frame and the velocity due to rotation of the frame.

$$\mathbf{v} = (\mathbf{v})_{Gx'y'} + \boldsymbol{\omega} \times \mathbf{r}' + \mathbf{v}_G. \quad (5)$$

Here, $\mathbf{r}' = x'\mathbf{e}_x + y'\mathbf{e}_y$ is the position of the flagellar element in the body-fixed frame. Next, the absolute velocity is expressed in terms of normal and tangential coordinates,

$$\mathbf{v} = v_N \mathbf{e}_N + v_T \mathbf{e}_T. \quad (6)$$

The tangent unit vector is $\mathbf{e}_T = \mathbf{g}_T / |\mathbf{g}_T|$, where $\mathbf{g}_T = d\mathbf{r}/ds$, and the normal unit vector \mathbf{e}_N is defined by $\mathbf{e}_T \cdot \mathbf{e}_N = 0$, and $\mathbf{e}_T \times \mathbf{e}_N = \mathbf{e}_z$.

Force/unit length is obtained directly from the equations

$$\mathbf{f} = f_N \mathbf{e}_N + f_T \mathbf{e}_T, \quad (7a)$$

$$f_N = C_N v_N, \quad (7b)$$

$$f_T = C_T v_T. \quad (7c)$$

Estimation of resistive force coefficients from the conditions of equilibrium

The values of the resistive-force coefficients are determined by ensuring that the conditions of equilibrium are satisfied. The fluid forces on the flagellum must balance the viscous drag forces on the cell body (Fig. 3). In a similar way, the net moment of the fluid forces on the flagellum must balance the moment exerted by the fluid on the rotating cell body. In this simplified analysis, we neglect the long-range effects of each part of the system (body or flagellum) on the flow around the other part.

First, the specific force on the flagellum is integrated along the length of the flagellum to estimate the net force:

$$\mathbf{F}_f = \int_0^L \mathbf{f} ds, \quad (8)$$

$$\mathbf{F}_f = F_{xf} \mathbf{e}_x + F_{yf} \mathbf{e}_y. \quad (9)$$

In a similar way, the net moment of the fluid forces on the flagellum, about the center of the cell, which is also the origin of the body-fixed frame, is

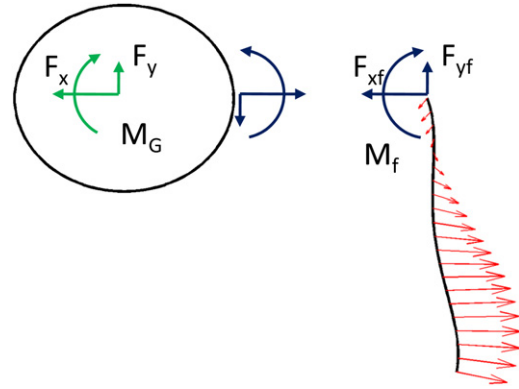


FIGURE 3 Free body diagrams of the cell and flagellum. If inertial effects are neglected, the forces exerted by the flagellum on the cell body are exactly balanced by the viscous drag due to translation and rotation of the body.

$$\mathbf{M}_{Gf} = \int_0^L \mathbf{r}' \times \mathbf{f} ds. \quad (10)$$

This torque can also be expressed in terms of the net moment, \mathbf{M}_f , about the origin of the flagellum (r_f (Fig. 3)).

$$\mathbf{M}_{Gf} = \mathbf{M}_f + \mathbf{r}_f \times \mathbf{F}_f, \quad (11)$$

where

$$\mathbf{M}_f = \int_0^L (\mathbf{r}' - \mathbf{r}_f) \times \mathbf{f} ds. \quad (12)$$

Applying the equations governing an ellipsoid in Stokes flow (Eqs. 3a–3f), the predicted linear and angular velocities of the cell body, given these flagellar forces and moments, would be

$$v_{xf} = \frac{F_{xf}}{6\pi\mu a C_{F1}}, \quad (13a)$$

$$v_{yf} = \frac{F_{yf}}{6\pi\mu a C_{F2}}, \quad (13b)$$

$$\omega_f = \frac{M_{Gf}}{8\pi\mu a b^2 C_{F3}}. \quad (13c)$$

Equations 13a–13c for the drag on an ellipsoid assume that the body is moving in an infinite fluid domain. In fact, the cell is swimming in a space bounded by two walls: the microscope slide and the coverslip. One or both of these boundaries may influence the translation of the cell. The lower surface is likely to be important, since we observe that unflagellate *Chlamydomonas* do not swim effectively and are found near the bottom of the fluid volume. We observe that the resistive force coefficients that produce the best fit to the angular velocity of the cell (using Eq. 13c) overestimate both components of the linear velocity of the cell, obtained via Eqs. 13a and 13b. This is likely because the cell body is relatively large in comparison to its distance from one or both of the rigid boundaries, so that the effects of the boundaries cannot be neglected. Studies of the motion of a sphere in viscous fluid bounded by one or two walls (31–33) show that the relationship between torque and angular rotation is barely affected by the boundaries, whereas the relationship between force and linear velocity is strongly affected. A simple approximation is proposed to account for this effect: the viscosity in the equations for linear motion of

the ellipsoid is increased by a boundary correction factor, α . Eqs. 13a–13c are replaced by:

$$v_{xf} = \frac{F_{xf}}{\alpha 6\pi\mu\alpha C_{F1}}, \quad (14a)$$

$$v_{yf} = \frac{F_{yf}}{\alpha 6\pi\mu\alpha C_{F2}}, \quad (14b)$$

$$\omega_f = \frac{M_{Gf}}{8\pi\mu ab^2 C_{F3}}. \quad (14c)$$

A value of α was found (Supporting Material) at which the predicted translational and angular velocities simultaneously agree well with measured values. For each cell, at a given value of α , there exist coefficients C_{NA} and C_{TA} that minimize the total normalized mean-squared error, E , in both linear and angular velocity predictions. Under the same conditions, there are different coefficients, C_{NR} and C_{TR} , that minimize the normalized mean-squared error, E_R , in the predicted angular velocity alone. At an appropriate value of α the values of these coefficients are similar ($C_{NR}/C_{NA} \approx 1$) and the total normalized mean-squared error, E , is small, so that good predictions are obtained for both angular and linear velocity.

The specific values of the resistive-force coefficients are obtained by an optimization procedure. The coefficients C_N and C_T in Eqs. 7a–7c are varied systematically in the range of 5–350 pN-s/ μm^2 . For each pair of values, the linear and angular velocities of the cell body predicted from the motion of the flagellum by Eqs. 4–14 are compared to the values measured directly by digital image correlation of the cell body. Agreement is measured by the normalized mean-squared error:

$$E_R = \int_0^T (\omega - \omega_f)^2 d\tau / \int_0^T \omega^2 d\tau, \quad (15a)$$

$$E_x = \int_0^T (v_x - v_{xf})^2 d\tau / \int_0^T v_x^2 d\tau, \quad (15b)$$

$$E_y = \int_0^T (v_y - v_{yf})^2 d\tau / \int_0^T v_y^2 d\tau, \quad (15c)$$

$$E = E_R + E_x + E_y. \quad (15d)$$

The values of the resistive-force coefficients that produce the smallest normalized mean-squared error using Eqs. 4–15 are considered to be the optimal estimates.

RESULTS

Overview of cell kinematics

Videos of nine *uni1-2* (wild-type) cells, nine *uni1-2; ida3* (*ida3*) cells, and 15 *uni1-2; oda2* (*oda2*) cells were analyzed. Each video met the following criteria: it must contain at least 200 frames, each of which is a full image of a counterclockwise rotating cell with a distinct (dark) flagellum. One wild-type cell, one *ida3* cell and two *oda2* cells were eliminated because their behavior was nonperiodic or otherwise qualitatively different from others (possible reasons are the health of the cell, or interactions with debris). Representative flagellar waveforms (one wild-type cell, one *ida3* cell and two *oda2* cells) were eliminated because their behavior was nonperiodic or otherwise qualitatively different from others (possible reasons are the health of the cell, or interactions with debris). Representative flagellar waveforms ($x'(s,t)$ versus $y'(s,t)$) of *Chlamydomonas* cells (wild-type, *ida3*, and *oda2*) are shown in Fig. 4 (top row). The shape of the flagellum is depicted along with the ellipsoidal cell body at 10 instants during the flagellar beat. The cell moves to the right and rotates counterclockwise in response to this stroke. Fig. 4 further shows the time series of angular position (*middle row*), as well as the power spectral density function of angular displacement (*bottom row*) estimated from the averaged FFT magnitudes of overlapping

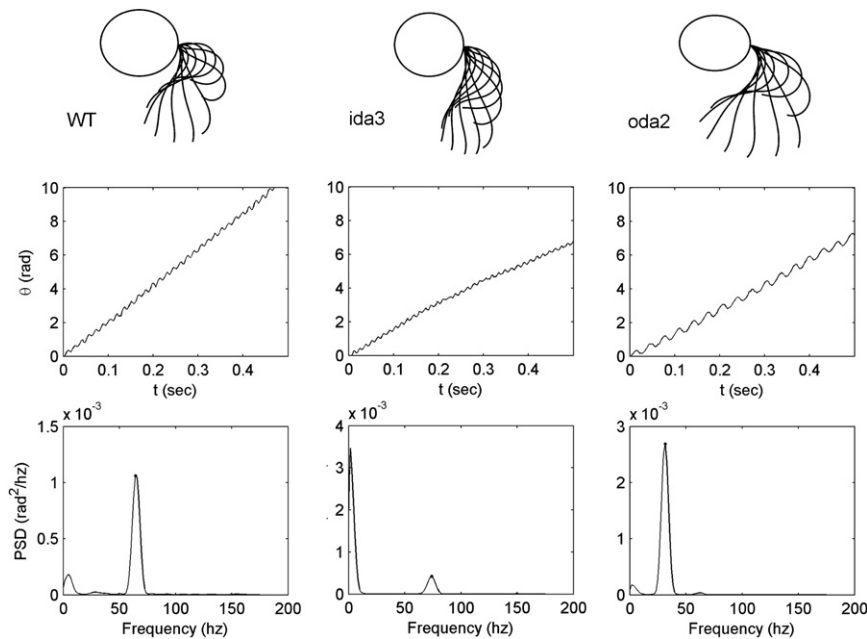


FIGURE 4 (Top row) Flagellar waveforms for typical wild-type (WT), *ida3*, and *oda2* uniflagellate *Chlamydomonas* cells. (Middle row) Angular position of the cell body plotted versus time for wild-type, *ida3*, and *oda2* cells. (Bottom row) The power spectral density (PSD) function estimated from the corresponding time series above. The mid-range peak in the power spectral density occurs at the characteristic beat frequency.

segments, for the three cells in the top row. The waveform of the *ida3* cell is noticeably abbreviated in comparison to wild-type and *oda2* waveforms. The beat frequency of the *oda2* cell is significantly lower than that of the other two. These features—stunted waveform in *ida3* and low beat frequency in *oda2*—both lead to lower rates of rotation. The basic statistics of the swimming behavior of these three groups of cells are contained in Table 1; the differences depicted in Fig. 4 occur consistently.

Fig. 5 shows the results of various steps in the analysis of the cell-body motion. Fig. 5, *a–c*, shows the linear and angular displacement, with respect to the laboratory frame, of the center of the cell. Fig. 5, *d–f*, contains the time series of velocity components v_x and v_y , obtained by numerical differentiation of X and Y followed by transformation into the body-aligned frame. Fig. 5, *g–i*, shows v_x and v_y after sorting by phase in the flagellar beat. Also shown are the low-pass-filtered versions of these time series.

The flagellar beat contains propulsive (power stroke) and recovery stages. Fig. 6 illustrates the qualitative correspondence between the stages of the flagellar beat and the kinematics of the cell body. Fig. 6, *a–c*, shows the filtered time series of angular and linear velocity of the cell; Fig. 6 *d* illustrates the waveform of the flagellum at eight equally spaced phases of the beat, so that each waveform is depicted roughly underneath the data obtained at that instant. The power stroke of the flagellum, which is the fast clockwise rotation of the extended flagellum, coincides with the maximum counterclockwise rotation and forward (x) velocity of the body. The recovery stroke corresponds to periods of slower (or negative) rotation and slower forward (or backward) translation.

Forces on the flagellum and cell body

Quantitative estimates of local velocity and specific force vectors are shown in Fig. 7; both quantities are vector functions of axial position along the flagellum. These velocity vectors are calculated with respect to the laboratory frame, and include the contributions of flagellar motion with respect to the body-fixed frame, the translation of the frame

TABLE 1 Geometric and kinematic statistics (mean \pm SD) for uniflagellate wild-type, *ida3*, and *oda2* cells

	WT ($n = 8$)	<i>ida3</i> ($n = 8$)	<i>oda2</i> ($n = 13$)
R_{avg} (μm)	4.01 ± 0.39	3.56 ± 0.37	3.19 ± 0.47
e	0.48 ± 0.13	0.59 ± 0.15	0.61 ± 0.17
L (μm)	12.4 ± 1.4	11.9 ± 1.5	12.1 ± 1.8
Ω_B (beats/s)	67.2 ± 8.0	59.8 ± 13.8	30.8 ± 3.0
Ω_R (rev/s)	4.51 ± 1.07	2.28 ± 0.43	2.19 ± 0.56
θ_{RMS} (rad)	0.678 ± 0.050	0.518 ± 0.048	0.602 ± 0.046

R_{avg} , average radius of ellipsoid; e , eccentricity of elliptical cross-section; L , flagellar length; Ω_B , beat frequency; Ω_R , rotation frequency; θ_{RMS} , root-mean-square amplitude of θ (the tangent angle of the flagellum) over the entire length of the flagellum and period of the beat.

itself, and the effect of the rotation of the frame (Eq. 5). The normal and tangential components of velocity at each point are multiplied by the corresponding resistive-force coefficients to produce the local (vector) force per unit length.

Comparisons of measured and predicted angular and linear velocities are shown in Fig. 8. Data from one cell of each type (wild-type, *ida3*, and *oda2*) are shown. The measured angular and linear velocities of the cell body were obtained by numerical differentiation of displacements, transformation into the body-aligned frame, sorting, and filtering. The predicted velocities are obtained by integrating the estimated forces on the flagellum (c.f., Fig. 6) and substituting the net forces and moment into the equations governing an ellipsoid in Stokes flow between two rigid planes (Eqs. 14a–14c). In each of the comparisons shown in Fig. 8, the viscosity of the medium at 21°C was $\mu \approx 1.0 \times 10^{-3} \text{ pN}\cdot\text{s}/\mu\text{m}^2$, and the boundary correction factor for the cell body was set to $\alpha = 2.0$, which was found to allow simultaneously accurate predictions for both angular and linear velocity components (Supporting Material). The values of the resistive-force coefficients were those found to produce the least mean-squared error between actual and predicted motion. The agreement is good, although some discrepancies are visible, most notably in v_y . The best agreement, both qualitatively and quantitatively, is seen in the *oda2* cell.

The values of the resistive-force coefficients estimated for each type of cell are shown in Fig. 9 *a*. There is no significant difference between the values estimated for wild-type and *ida3* cells, although the kinematics of the waveform, and of the cell body are quite different. The values of the resistive-force coefficients for *oda2* exhibit differences from wild-type and *ida3* that are statistically significant (by one-way analysis of variance), but relatively small, despite the large difference in beat frequency. The overall mean (\pm SD) values of the coefficients are $C_N = (1.54 \pm 0.50) \times 10^{-3} \text{ pN}\cdot\text{s}/\mu\text{m}^2$ and $C_T = (0.68 \pm 0.26) \times 10^{-3} \text{ pN}\cdot\text{s}/\mu\text{m}^2$. The plots of average normalized mean-squared error reflect good qualitative agreement between measured linear and angular velocities and the corresponding velocities predicted by resistive-force theory. Residual error statistics (Fig. 9 *b*) suggest that the resistive-force theory performs slightly better for *oda2* cells than for WT or *ida3* cells.

DISCUSSION

The primary aim of this study is to estimate the distributed forces on the flagellum of *Chlamydomonas reinhardtii* throughout its beat. The kinematics of the cell body and flagellum are obtained by analysis of images of uniflagellate cells obtained by high-speed video microscopy. The equations governing the motion of an ellipsoid in Stokes flow are used to estimate the forces on the cell body required

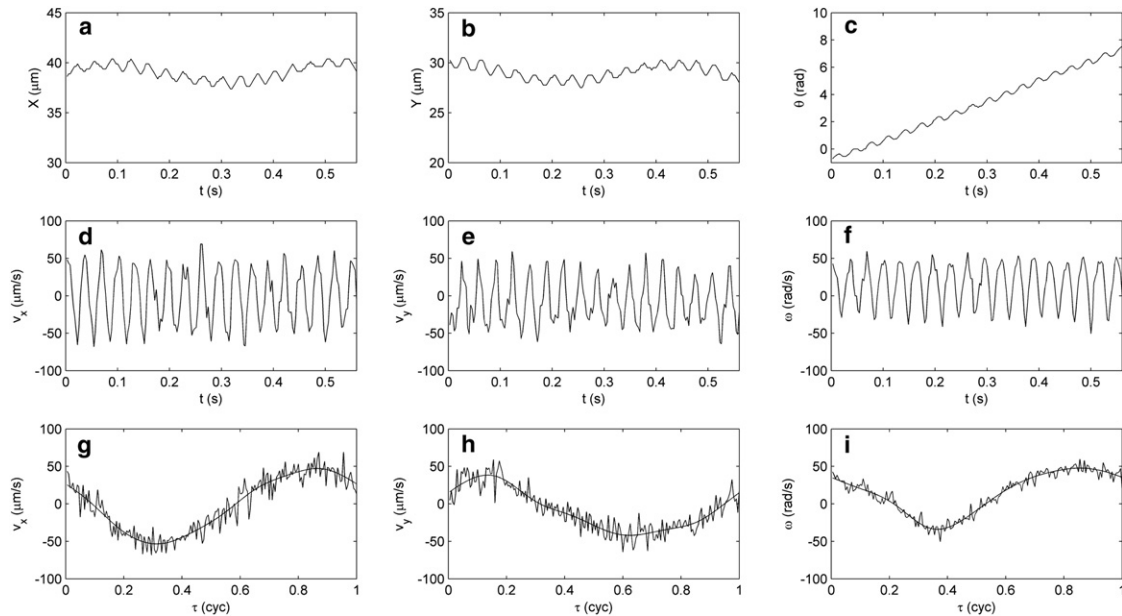


FIGURE 5 (a–c) Displacement (X , Y components with respect to the laboratory frame) of the center of the cell body, and the angle of rotation of the cell body relative to the original position and orientation. (d–f) Velocity components (v_x , v_y) of the cell body with respect to the body-aligned frame; angular velocity of the cell body, ω . Data are shown as a function of time. (g–i) Linear and angular velocity of the cell, sorted by relative phase in the flagellar beat. Smooth estimates of linear and angular velocity obtained by low-pass filtering are superimposed on the raw (sorted) data.

to produce observed translation and rotation. Resistive-force theory is used to describe the forces on the flagellum, and the resistive coefficients are estimated from the conditions of force equilibrium.

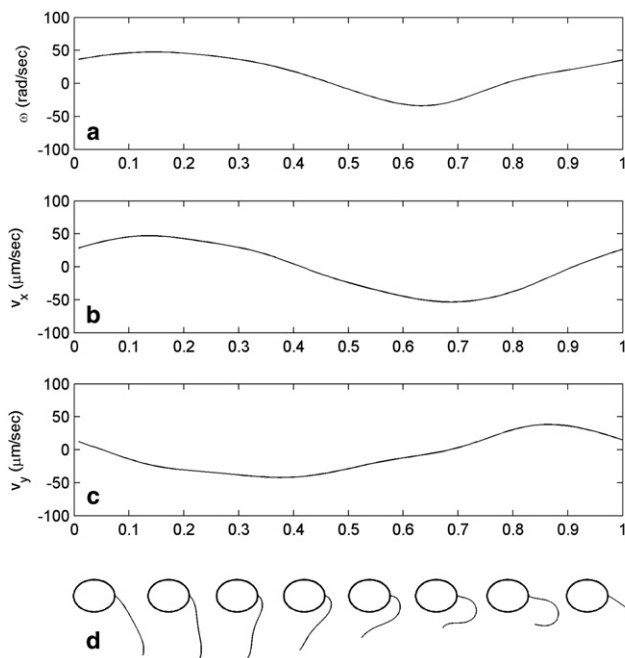


FIGURE 6 (a–c) Angular and linear velocity of the cell body (the latter with respect to the body-aligned frame) for a sample cell, shown as a function of relative phase in the flagellar beat cycle. (d) Position of the flagellum at eight equally-spaced phases of the beat aligned with the time series in a–c.

The flow field around the biflagellate *Chlamydomonas* has been discussed in recent articles by Guasto et al. (29) and by Drescher et al. (30). These studies illuminate the motion of the fluid but do not directly address the magnitude, timing, or spatial distribution of force on the flagellum. They do describe kinematic measurements of the cell body that are comparable to those of the current study, and calculate the power dissipated by the fluid. In biflagellate cells, Guasto and colleagues (29) obtain oscillatory velocities of the cell body approximately four times larger than those observed in uniflagellate cells in this study. Half this difference may be explained by the number of flagella. We propose that the remaining factor of ~ 2 may be due to greater boundary effects in this study (the poorly swimming uniflagellate flagellum swims within one or two body diameters of the lower boundary). Estimates of power dissipated by viscous drag and torque on the cell body are readily obtained from their products with velocity and angular velocity, respectively. Average (\pm SD) power dissipation is 4.90 ± 1.66 fW for wild-type cells, 1.39 ± 0.45 fW for *ida3* cells, and 1.01 ± 0.56 fW for *oda2* cells. The estimate of average power dissipation obtained by Guasto et al. (29) from the gradient of the velocity field is ~ 5 fW (see Fig. 4 of Guasto et al. (29)).

The effects of rigid-plane boundaries (slide and coverslip) on the motion of the cell were accounted for by a boundary correction factor, α . Selection of a unique, appropriate value for α is enabled by the simultaneous measurement of angular and linear velocity of the cell body. Only at the appropriate value of α will the predicted angular velocity be consistent with the predicted linear velocity, because

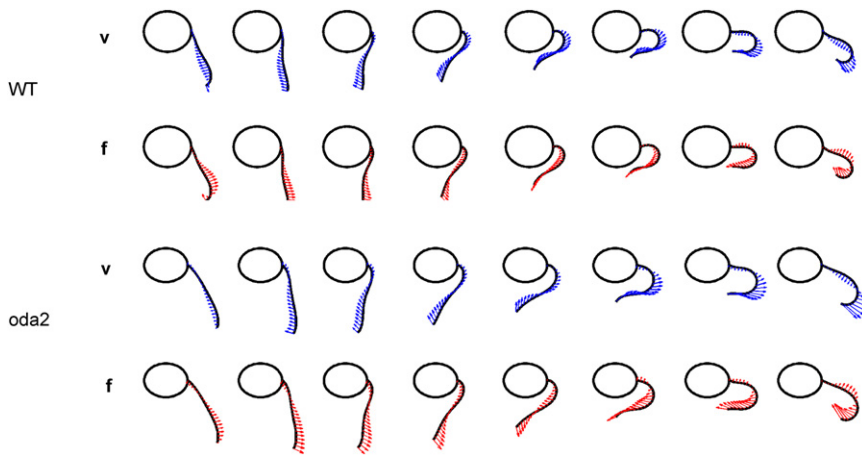


FIGURE 7 Estimates of velocity (v) and force (f , per unit length) exerted by the fluid on the flagellum of *Chlamydomonas* in wild-type (WT) and outer-arm-deficient (*oda2*) cells. Velocity vectors (v) are calculated with respect to the laboratory frame of reference. Velocities are obtained by numerical differentiation of the flagellar coordinates in the body-fixed frame, plus addition of terms due to translation and rotation of the body-fixed frame. Force vectors (f) are estimated by multiplying the normal and tangential velocity components, v_N and v_T , by corresponding resistive coefficients C_N and C_T . For the wild-type cell, $C_N = 1.53 \times 10^{-3} \text{ pN}\cdot\text{s}/\mu\text{m}^2$ and $C_T = 0.64 \times 10^{-3} \text{ pN}\cdot\text{s}/\mu\text{m}^2$. For the *oda2* cell, $C_N = 1.62 \times 10^{-3} \text{ pN}\cdot\text{s}/\mu\text{m}^2$ and $C_T = 0.71 \times 10^{-3} \text{ pN}\cdot\text{s}/\mu\text{m}^2$.

the relationship between force and linear velocity is strongly affected by boundary effects, but the relationship between torque and angular velocity is not. For example, a sphere of radius R moving between two walls separated by $3R$ would experience 2.4 times the linear drag on the same sphere moving at the same speed in an infinite domain (31). In contrast, the viscous torque on a sphere of radius R rotating between two plane boundaries $3R$ apart would experience a viscous torque only ~ 1.05 times greater than the same sphere rotating in an infinite domain (32). In summary, several observations support the use of a to capture boundary effects: the propensity of unflagellate *Chlamydomonas* to swim near the lower boundary; the comparison of cell-body velocity with velocities observed

in other studies (29), the consistency of the optimal value of a among all cells, the similarity between estimated resistive force coefficients, and the consistent minimization of residual error at this value. Accounting for boundary effects should provide better estimates of the magnitudes of viscous forces and resistive coefficients than direct applications of the formulas governing ellipsoid motion in an infinite domain (Eqs. 13a–13c) (34).

Lighthill (17) provides an authoritative analysis of flagellar locomotion. Lighthill advocates alternatives to resistive-force theory, but he also provides theoretical estimates of the coefficients C_N and C_T (his K_N and K_T) by analyzing a distribution of what he calls stokeslets along the centerline of the flagellum:

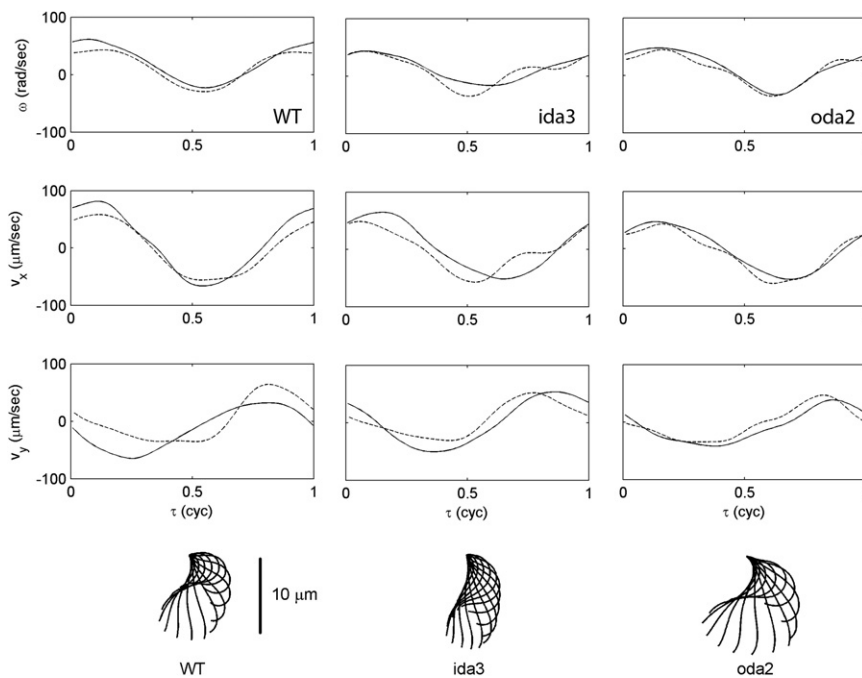


FIGURE 8 Comparison of measured angular and linear velocities of the cell body (solid lines) with values predicted by a mathematical model of an ellipsoid in Stokes flow (dashed lines). In the mathematical model, the net forces and moments on the flagellum are estimated by integrating fluid forces along the length of the flagellum. The net flagellar forces and moments are applied to a prolate ellipsoid with major and minor axes measured in the image plane. The normal and tangential components of the distributed force on the flagellum are estimated from the corresponding velocity components of the flagellum multiplied by resistive-force coefficients. The coefficients that produce the best agreement (smallest mean-squared error) between measured and modeled motion of the cell body are used to produce the dashed curve. Column 1, a wild-type cell ($C_N = 1.53 \times 10^{-3}$, $C_T = 0.64 \times 10^{-3} \text{ pN}\cdot\text{s}/\mu\text{m}^2$; $E = 0.204$); Column 2, an *ida3* mutant ($C_N = 1.01 \times 10^{-3} \text{ pN}\cdot\text{s}/\mu\text{m}^2$; $C_T = 0.55 \times 10^{-3} \text{ pN}\cdot\text{s}/\mu\text{m}^2$; $E = 0.156$); Column 3, an *oda2* mutant cell ($C_N = 1.62 \times 10^{-3} \text{ pN}\cdot\text{s}/\mu\text{m}^2$; $C_T = 0.71 \times 10^{-3} \text{ pN}\cdot\text{s}/\mu\text{m}^2$; $E = 0.123$).

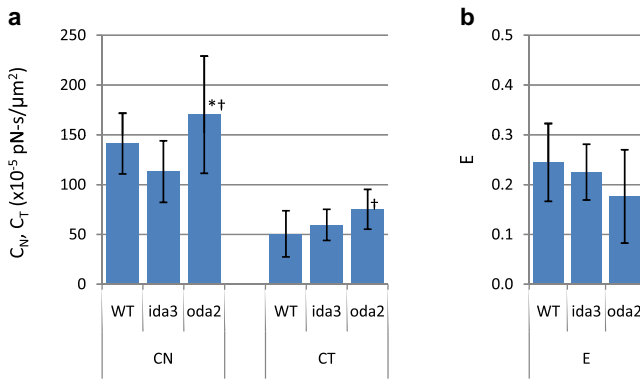


FIGURE 9 (a) Mean values (\pm SD) of the resistive-force coefficients that produce the closest agreement between measured and predicted velocities of the cell body, for wild-type, *ida3*, and *oda2* cells ($\alpha = 2.0$). Statistical significance ($p < 0.05$) is denoted by † (different from wild-type) or * (different from *ida3*). (b) Normalized mean-squared error between measured and predicted velocities of *Chlamydomonas* cell bodies. A normalized mean-squared error of $E = 0$ corresponds to perfect agreement; $E = 1$ corresponds to poor prediction (mean-squared error equal to the variance of the data). The overall mean (\pm SD) values of the coefficients are $C_N = (1.54 \pm 0.50) \times 10^{-3} \text{ pN}\cdot\text{s}/\mu\text{m}^2$; $C_T = (0.68 \pm 0.26) \times 10^{-3} \text{ pN}\cdot\text{s}/\mu\text{m}^2$; overall error, $E = 0.20 \pm 0.08$.

$$C_N = \frac{4\pi\mu}{\ln\left(\frac{2q}{r}\right) + 1/2}, \quad (16a)$$

$$C_T = \frac{2\pi\mu}{\ln\left(\frac{2q}{r}\right)}, \quad (16b)$$

where r is the radius of the flagellum and q is a characteristic length. The value of q is not uniquely specified, but Lighthill suggests that $q = 0.09\Lambda$, where Λ is the wavelength of the sinusoidal flagellar shape. It is not clear what the wavelength Λ or value of q should be for the asymmetric waveform of the *Chlamydomonas* flagellum. If Lighthill's formulas are applied with $r = 120 \text{ nm}$ (35) and $\Lambda = 2L$ ($q \approx 2.4 \mu\text{m}$), we obtain $C_N \approx 3.0\mu$ and $C_T \approx 1.7\mu$. These values are roughly twice the experimental estimates of the current study.

Johnson and Brokaw (18) evaluated resistive-force theory in simulations of flagellar motion and compared it to the more accurate slender-body theory of flagellar propulsion espoused by Cox (19) and Batchelor (20). Johnson and Brokaw (18) conclude that close agreement between observed and predicted motion of the cell body would not be obtained from simple resistive-force theory because of long-range interactions between cell body and flagellum. However, the predictions of resistive-force theory, although not as accurate as those of slender-body theory, were in fact able to predict simulated results reasonably well. The good agreement observed in this study between cell motion and motion predicted by simple resistive-force theory supports its use for practical first-order analyses. Residual error is probably largely due to the neglected long-range interactions between the body and the

flagellum. We hypothesize that this interaction is somewhat less for the slower-beating *oda2* cells, leading to better approximation by resistive-force theory. These long-range hydrodynamic interactions, though they appear to have a minor effect on the magnitude of propulsive forces, may be very important to the synchronization of two or more flagella (36,37).

Using digital analysis of high-speed video, Friedrich and co-authors (34) analyzed the more symmetric and sinusoidal waveform of the bull-sperm flagellum. They found resistive-force coefficients $C_N \approx 1.8\mu$ and $C_T \approx \mu$ (where the viscosity is $\mu \approx 0.7 \times 10^{-3} \text{ pN}\cdot\text{s}/\mu\text{m}^2$ for water at 36°C). They did not apply any correction for surface boundary effects (perhaps because they were less significant). Because of the slower beat frequency of the bull-sperm flagella, their data did not require sorting. It is noteworthy that the resistive-force coefficients estimated by Friedrich et al. (34) for the bull sperm are very close to those obtained for the *Chlamydomonas* flagellum in this study, especially if scaled by the temperature-dependent viscosity. Both sets of estimates are slightly smaller than the theoretical predictions of Lighthill. The similarity between sets of resistive force coefficients is noteworthy when one considers the differences in the two experimental models. The bull-sperm flagellum pushes the head forward, whereas the *Chlamydomonas* flagellum pulls the cell body behind it. Furthermore, the bull-sperm flagellum is four to five times as long ($50 \mu\text{m}$) as the *Chlamydomonas* flagellum ($12 \mu\text{m}$) and of varying diameter, roughly twice the $\sim 200\text{-nm}$ diameter of *Chlamydomonas*.

Wild-type, inner-arm deficient (*ida3*), and outer-arm deficient (*oda2*) cells were analyzed in this study. Coefficients estimated from the stunted waveform of *ida3* and from the slower flagellar beat of *oda2* were very similar to those estimated from the normal flagellar beat of wild-type cells. This consistency among phenotypes provides confidence in the approach and the estimates themselves. The force estimates from this study can be used with complementary information on the flexural rigidity of the axoneme, to arrive at accurate estimates of the internal forces produced within the axoneme (Fig. S2).

CONCLUSION

This study provides a comprehensive description of the kinematics and kinetics of flagellar propulsion in *Chlamydomonas reinhardtii*. We find that the propulsive forces on the flagellum are well approximated by resistive-force theory. The results are specific and quantitative and thus provide important information needed to unravel the mechanics and coordination of cilia and flagella.

SUPPORTING MATERIAL

Methods and Materials, references, three movies, and raw data are available at [http://www.biophysj.org/biophysj/supplemental/S0006-3495\(11\)00557-1](http://www.biophysj.org/biophysj/supplemental/S0006-3495(11)00557-1).

Funding for this work was provided by the Children's Discovery Institute.

REFERENCES

1. Summers, K. E., and I. R. Gibbons. 1971. Adenosine triphosphate-induced sliding of tubules in trypsin-treated flagella of sea-urchin sperm. *Proc. Natl. Acad. Sci. USA.* 68:3092–3096.
2. Lindemann, C. B. 1994. A model of flagellar and ciliary functioning which uses the forces transverse to the axoneme as the regulator of dynein activation. *Cell Motil. Cytoskeleton.* 29:141–154.
3. Lindemann, C. B. 2004. Testing the geometric clutch hypothesis. *Biol. Cell.* 96:681–690.
4. Gennerich, A., A. P. Carter, ..., R. D. Vale. 2007. Force-induced bidirectional stepping of cytoplasmic dynein. *Cell.* 131:952–965.
5. Huang, B., Z. Ramanis, ..., D. J. Luck. 1982. Uniflagellar mutants of *Chlamydomonas*: evidence for the role of basal bodies in transmission of positional information. *Cell.* 29:745–753.
6. Brokaw, C. J., D. J. Luck, and B. Huang. 1982. Analysis of the movement of *Chlamydomonas* flagella: the function of the radial-spoke system is revealed by comparison of wild-type and mutant flagella. *J. Cell Biol.* 92:722–732.
7. Brokaw, C. J., and D. J. Luck. 1983. Bending patterns of *chlamydomonas* flagella I. Wild-type bending patterns. *Cell Motil.* 3:131–150.
8. Dutcher, S. K., W. Gibbons, and W. B. Inwood. 1988. A genetic analysis of suppressors of the PF10 mutation in *Chlamydomonas reinhardtii*. *Genetics.* 120:965–976.
9. King, S. J., W. B. Inwood, ..., S. K. Dutcher. 1994. The *bop2-1* mutation reveals radial asymmetry in the inner dynein arm region of *Chlamydomonas reinhardtii*. *J. Cell Biol.* 126:1255–1266.
10. Bower, R., K. VanderWaal, ..., M. E. Porter. 2009. IC138 defines a subdomain at the base of the II dynein that regulates microtubule sliding and flagellar motility. *Mol. Biol. Cell.* 20:3055–3063.
11. Brokaw, C. J. 1984. Automated methods for estimation of sperm flagellar bending parameters. *Cell Motil.* 4:417–430.
12. Brokaw, C. J., and R. Kamiya. 1987. Bending patterns of *Chlamydomonas* flagella: IV. Mutants with defects in inner and outer dynein arms indicate differences in dynein arm function. *Cell Motil. Cytoskeleton.* 8:68–75.
13. Kamiya, R. 1995. Exploring the function of inner and outer dynein arms with *Chlamydomonas* mutants. *Cell Motil. Cytoskeleton.* 32: 98–102.
14. Wirschell, M., T. Hendrickson, and W. S. Sale. 2007. Keeping an eye on II: II dynein as a model for flagellar dynein assembly and regulation. *Cell Motil. Cytoskeleton.* 64:569–579.
15. Nicastro, D., C. Schwartz, ..., J. R. McIntosh. 2006. The molecular architecture of axonemes revealed by cryoelectron tomography. *Science.* 313:944–948.
16. Gray, J., and G. J. Hancock. 1955. The Propulsion of Sea-Urchin Spermatozoa. *J. Exp. Biol.* 32:802–814.
17. Lighthill, J. 1976. Flagellar hydrodynamics (The John von Neumann Lecture, 1975). *SIAM Rev.* 18:161–230.
18. Johnson, R. E., and C. J. Brokaw. 1979. Flagellar hydrodynamics. A comparison between resistive-force theory and slender-body theory. *Biophys. J.* 25:113–127.
19. Cox, R. G. 1971. Motion of long slender bodies in a viscous fluid. Part 1. General theory. *J. Fluid Mech.* 44:791–810.
20. Batchelor, G. K. 1970. Slender-body theory for particles of arbitrary cross-section in Stokes flow. *J. Fluid Mech.* 44:419–440.
21. Holmes, J. A., and S. K. Dutcher. 1989. Cellular asymmetry in *Chlamydomonas reinhardtii*. *J. Cell Sci.* 94:273–285.
22. Dutcher, S. K. 1995. Mating and tetrad analysis in *Chlamydomonas reinhardtii*. *Methods Cell Biol.* 47:531–540.
23. Reference deleted in proof.
24. Lux, 3rd, F. G., and S. K. Dutcher. 1991. Genetic interactions at the FLA10 locus: suppressors and synthetic phenotypes that affect the cell cycle and flagellar function in *Chlamydomonas reinhardtii*. *Genetics.* 128:549–561.
25. Bayly, P. V., B. L. Lewis, ..., S. K. Dutcher. 2010. Efficient spatiotemporal analysis of the flagellar waveform of *Chlamydomonas reinhardtii*. *Cytoskeleton.* 67:56–69.
26. Rosenfeld, A., and K. A. Avinash. 1976. Digital Picture Processing. Academic Press, New York.
27. Oberbeck, A. 1876. Ueber stationäre Flüssigkeitsbewegungen mit Berücksichtigung der inneren Reibung. *J. reine angew. Math.* 81:62–80.
28. Chwang, A. T., and T. Y. T. Wu. 1975. Hydromechanics of low Reynolds number flows. Part 2. Singularity method for Stokes flows. *J. Fluid Mech.* 67:787–815.
29. Guasto, J. S., K. A. Johnson, and J. P. Gollub. 2010. Oscillatory flows induced by microorganisms swimming in two dimensions. *Phys. Rev. Lett.* 105:168102.
30. Drescher, K., R. E. Goldstein, ..., I. Tuval. 2010. Direct measurement of the flow field around swimming microorganisms. *Phys. Rev. Lett.* 105:168101.
31. Ganatos, P., R. Pfeffer, and S. Weinbaum. 1980. A strong interaction theory for the creeping motion of a sphere between parallel plane boundaries. Part 2. Parallel motion. *J. Fluid Mech.* 99:755–783.
32. Liu, Q. L., and A. Prosperetti. 2010. Wall effects on a rotating sphere. *J. Fluid Mech.* 657:1–21.
33. Happel, J., and H. Brenner. 1983. Low Reynolds Number Hydrodynamics: With Special Applications to Particulate Media. M. Nijhoff, The Hague, Amsterdam.
34. Friedrich, B. M., I. H. Riedel-Kruse, ..., F. Jülicher. 2010. High-precision tracking of sperm swimming fine structure provides strong test of resistive force theory. *J. Exp. Biol.* 213:1226–1234.
35. Lindemann, C. B., and D. R. Mitchell. 2007. Evidence for axonemal distortion during the flagellar beat of *Chlamydomonas*. *Cell Motil. Cytoskeleton.* 64:580–589.
36. Goldstein, R. E., M. Polin, and I. Tuval. 2009. Noise and synchronization in pairs of beating eukaryotic flagella. *Phys. Rev. Lett.* 103:168103.
37. Polin, M., I. Tuval, ..., R. E. Goldstein. 2009. *Chlamydomonas* swims with two “gears” in a eukaryotic version of run-and-tumble locomotion. *Science.* 325:487–490.